Path Planning for Robust Image-Based Visual Servoing

Youcef Mezouar, François Chaumette

▶ To cite this version:

HAL Id: inria-00072534

https://hal.inria.fr/inria-00072534

Submitted on 24 May 2006

INRIA

Path Planning for Robust Image-based Visual Servoing

Youcef Mezouar, François Chaumette

N˚4097

Janvier 2001

———— THÈME 3 ————

Rapport de recherche

Path Planning
for Robust Image-based Visual Servoing

Youcef Mezouar, François Chaumette

Thème 3 — Interaction homme-machine,
images, données, connaissances
Projet Vista

Abstract: Vision feedback control loop techniques are efficient for a large class of applications but they come up against difficulties when the initial and desired robot positions are distant. Classical approaches are based on the regulation to zero of an error function computed from the current measurement and a constant desired one. By using such approach, it is not obvious to introduce any constraint in the realized trajectories and to ensure the convergence for all the initial configurations. In this paper, we propose a new approach to resolve these difficulties by coupling path planning in image space and image-based control. Constraints such that the object remains in the camera field of view or the robot avoids its joint limits can be taken into account at the task planning level. Furthermore, by using this approach, current measurements always remain close to their desired value and a control by image-based servoing ensures the robustness with respect to modeling errors. The proposed method is based on the potential field approach and is applied when object shape and dimensions are known or not, and when the calibration parameters of the camera are well or badly estimated. Finally, real time experimental results using an eye-in-hand robotic system are presented and confirm the validity of our approach.

Key-words: Path planning, Visual servoing

(Résumé : tsvp)

Planification de trajectoires dans l'image pour un asservissement visuel robuste

Résumé :   Les techniques d'asservissement visuel sont efficaces pour une grande classe d'application mais se heurtent à des difficultés quand le déplacement à effectuer est trop important. Les approches classiques sont basées sur la régulation à zéro de l'erreur entre les valeurs courante et désirée d'information visuelles sélectionnées soit dans l'image, soit dans l'espace 3-D. Il est alors difficile d'introduire des contraintes sur la trajectoire réalisée et d'assurer la convergence quelle que soit la position initiale du robot. Dans ce rapport, on étudie le problème de la planification de trajectoire dans l'image et l'on propose une méthode permettant d'assurer la convergence quelle que soit le déplacement à réaliser en couplant génération de trajectoire et asservissement visuel dans l'image. La méthode proposée est basée sur l'utilisation de champs de potentiel et est appliquée lorsque l'objet considéré est de forme et de dimensions connues ou inconnues et au cas où les paramètres de la caméra sont bien ou mal estimés. Les problèmes de visibilité de l'objet et d'évitement des butées articulaires du robot sont également traités. Finalement, des résultats expérimentaux, obtenus en utilisant une caméra embarquée sur un robot à six degrés de liberté, confirment la validité de notre approche.

Mots-clé :   Planification de trajectoires, Asservissement visuel

Contents

1   Introduction

Classical approaches using visual information in feedback control loops are point to point-based, i.e the robot must reach a desired goal configuration starting from a given initial configuration. Needed information is reduced to the goal configuration and a globally stabilizing feedback is required. However, if the initial error is large, such a control may product an erratic behavior and/or large control effort, especially in the presence of modeling errors. Furthermore, keeping all the object in the camera field of view remains a not obvious task. Visual servoing schemes are local feedback control solutions. They thus require the definition of intermediate subgoals in the sensor space at the task planning level. This paper deals with the problem of path planning in image space and presents a complete solution to specify and to track image trajectories of an object observed by an eye-in-hand robotic system.

Position-based and image-based servoing are now well known approaches [19], [6], [8]. The first one [20], [14], based on the computation of a 3-D Cartesian error, requires a perfect CAD-model of the object and a calibrated camera to obtain unbiased pose estimation. The main advantage of this approach is that it controls directly the camera trajectory in the Cartesian space. However, there is no control in the image and some part of the object may get out of the camera field of view during servoing. Additionally, the computation at each iteration of the control loop of a 3-D error may lead to a strong sensitivity with respect to modeling errors and noise perturbations [1]. In the second approach, the error is directly measured in the image. That implies some degrees of robustness with respect to modeling errors and noise perturbations. On the other hand, such a control may lead to inadequate camera motion (not optimal or not physically valid camera trajectory) [1]. By composing the error function of 3-D Cartesian features and image features, Malis et *al* propose a globally stabilizing solution called *2 1/2 D* visual servoing for general setup [13]. However *2 1/2 D* visual servoing is relatively sensitive to measurement perturbation since an homography is computed at each iteration of the control loop to extract the Cartesian part of the error function.

It is well known that image-based servoing is locally stable and robust with respect to modeling errors and noise perturbations. The key idea of our work is thus to use the local stability and robustness of image-based servoing by specifying trajectories to follow in the image. Indeed, for a trajectory following, a local control solution works properly since current and desired configurations remain close. Moreover, for all the previously cited control schemes, keeping the whole object in the camera field of view and avoiding the robot joint limits during servoing remain a not obvious task and can involve the failure of the servoing. These essential issues can be easily introduced at the task planning level.

Only few papers deal with path planning in image space. For a very simple case (the world is supposed to be planar and the camera is one dimensional), Cowan and Koditschek describe in [3] a globally stabilizing method using navigation function. In [7], a trajectory generator using a stereo system is proposed and applied to obstacle avoidance. An alignment task using intermediate views of an object synthesized by image morphing is presented in [18]. A path planning for a straight-line robot translation observed by a weakly calibrated stereo

system, is performed in [17]. However, none of them were dealing with robustness issues. In previous work [15], we have proposed a potential field-based path planning generator that determines the trajectories in the image of a set of points lying on a planar target. In this paper, we generalize this method to the case of objects of any unknown shapes. It is a robust and stable method even if initial and desired robot positions are distant. Our approach consists of three phases. In the first one, the discrete geometric camera path (that ensures the physical validity of the robot trajectory) is performed as a sequence of N intermediate camera poses which approaches as much as possible a straight line translation. In this phase, the mechanical and visibility constraints are introduced. In the second one, the discrete geometric trajectory of the target in the image and the discrete geometric trajectory of the robot in the joint space are obtained from the camera path. Finally, continuous and derivable geometric paths in the image with an associated timing law are generated and tracked using an image-based control scheme. By using this approach, current visual features always remain close to their desired value and a control by image-based servoing ensures the robustness with respect to modeling errors and noise perturbations. Contrary to other approaches exploiting the robot redundancy [2], [16], the mechanical and visibility constraints can be ensured even if all the robot degrees of freedom are used to realize the task. Our path planning strategy is based on the potential field method [9], [10] and can be applied even if none 3-D model is available and even if the camera intrinsic parameters are badly estimated.

The paper is organized as follows. In Section 2, we recall some basic fundamentals. The method of path planning for a known object is presented in Section 3 and extended to the case where a 3-D model of the object is not available in Section 4. Camera calibration errors are also considered. In Section 5, a timing law is associated to the geometric path. In Section 6, we show how to use an image-based control approach to track the trajectories. The experimental results are given in Section 7.

2 Fundamentals

In this section, we introduce notations and concepts that are necessary to design our path planning generator.

2.1 General description and notation

Let $\mathcal{F}_o$ be a frame attached to the target, $\mathcal{F}_i$, $\mathcal{F}_k$ and $\mathcal{F}_*$ be the frames attached to the camera in its initial, current and desired positions respectively (see Figure 2). $\mathcal{M}^j$ denotes a 3-D target point with homogeneous coordinates $\mathbf{M}_x^j = [\widetilde{\mathbf{M}}_x^{jT}\,1]^T = [X_x^j\,Y_x^j\,Z_x^j\,1]^T$ [1] in $\mathcal{F}_x$ (with $x \in \{o,\,i,\,k,\,*\}$). $\mathcal{M}^j$ is projected in the image at time k onto a point with homogeneous normalized coordinates $\mathbf{m}_k^j = [x_k^j\,y_k^j\,1]^T$. The corresponding coordinates in pixels are denoted $\mathbf{p}_k^j = [u_k^j\,v_k^j\,1]^T = [\widetilde{\mathbf{p}}_k^{jT}\,1]^T = \mathbf{A}m_k^j$, where the matrix $\mathbf{A}$ is a non singular

---

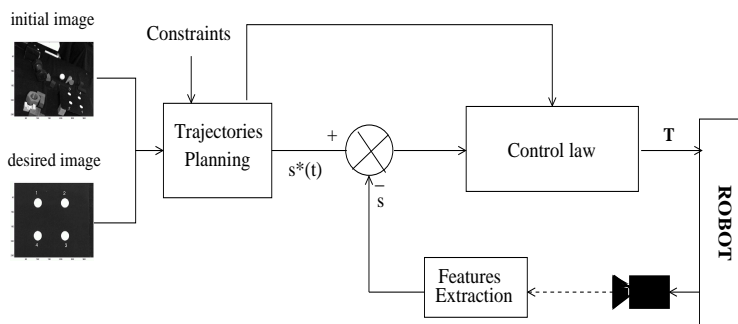[1] $\mathbf{A}^T$ denotes the transpose of the $\mathbf{A}$-matrix

Figure 1: Block diagram of the proposed method

matrix containing the camera internal parameters:

$$\mathbf{A} = \left[\begin{array}{ccc} fp_u & -fp_u cot(\theta) & u_0 \\ 0 & fp_v/sin(\theta) & v_0 \\ 0 & 0 & 1 \end{array} \right] = \left[\begin{array}{ccc} \alpha_u & \alpha_{uv} & u_0 \\ 0 & \alpha_v & v_0 \\ 0 & 0 & 1 \end{array} \right]$$

where u_0 and v_0 are the pixels coordinates of principal point, f is the focal length, p_u and p_v are the magnifications respectively in the u and v directions and θ is the angle between these axes.

The aim of our work is to design a trajectories generator performing a continuous and derivable curve $\mathbf{s}(t) = [\widetilde{\mathbf{p}}_{(t)}^{1^T} \cdots \widetilde{\mathbf{p}}_{(t)}^{n^T}]^T$ between the initial configuration $\mathbf{s}_i = [\widetilde{\mathbf{p}}_i^{1^T} \cdots \widetilde{\mathbf{p}}_i^{n^T}]^T$ and the desired one $\mathbf{s}_* = [\widetilde{\mathbf{p}}_*^{1^T} \cdots \widetilde{\mathbf{p}}_*^{n^T}]^T$. First, the discrete geometric camera path is performed as a sequence of N intermediate camera poses $\tau = \{ \Upsilon_k \ / \ k \in 1 \cdots N \}$ using the potential field strategy described in the next subsection. Then, the discrete object trajectory in the image $\mathcal{S} = \{ \mathbf{s}_k \ / \ k \in 1 \cdots N \}$ and the robot trajectory in the joint space $\mathcal{Q} = \{ \mathbf{q}_k \ / \ k \in 1 \cdots N \}$ are obtained from τ. Finally, continuous and derivable geometric path in the image with an associated timing law $\mathbf{s}(t)$ is performed and tracked (see Figure 1).

2.2   Potential field method

Our path planning strategy is based on the potential field method. This method was originally developed for an on-line collision avoidance [9], [10].

Classical approach

In this approach the robot motions are under the influence of an artificial potential field (V) defined as the sum of an attractive potential (V_a) pulling the robot towards the goal configuration (Υ_*) and a repulsive potential (V_r) pushing the robot away from the obstacles. Motion planning is performed in an iterative fashion. At each iteration an artificial force $\mathbf{F}(\Upsilon)$, where the 6×1 vector Υ represents a parameterization of the

robot workspace $\mathcal{W} \subset \mathbf{R}^p$, is induced by the potential function. This force is defined as $\mathbf{F}(\mathbf{\Upsilon}) = -\vec{\nabla}_{\mathbf{\Upsilon}}^T V$ where $\vec{\nabla}_{\mathbf{\Upsilon}}^T V$ denotes the transpose of the gradient vector of V at $\mathbf{\Upsilon}$. Using these conventions, $\mathbf{F}(\mathbf{\Upsilon})$ can be decomposed as the sum of two vectors, $\mathbf{F}_a(\mathbf{\Upsilon}) = -\vec{\nabla}_{\mathbf{\Upsilon}}^T V_a$ and $\mathbf{F}_r(\mathbf{\Upsilon}) = -\vec{\nabla}_{\mathbf{\Upsilon}}^T V_r$, which are respectively called the attractive and repulsive forces. Path generation proceeds along the direction of $\mathbf{F}(\mathbf{\Upsilon})$ regarded as the most promising direction of motion. Thus, each segment is oriented along the negated gradient of the potential function computed at the configuration attained by the previous segment. The discrete-time trajectory is given by the transition equation:

$$\mathbf{\Upsilon}_{k+1} = \mathbf{\Upsilon}_k + \varepsilon_k \frac{\mathbf{F}(\mathbf{\Upsilon}_k)}{\|\mathbf{F}(\mathbf{\Upsilon}_k)\|} \tag{1}$$

where k is the increment index and ε_k is a positive scaling factor denoting the length of the kth increment.

Modified Forces

Consider the unconstrained problem:

$$min\, V(\mathbf{\Upsilon}), \quad \mathbf{\Upsilon} \in \mathbf{R}^p$$

A classical continuous gradient strategy for finding a minimum of V consists of making $\mathbf{\Upsilon}(t)$ vary according to the evolution equation:

$$\dot{\mathbf{\Upsilon}} = -\epsilon \mathbf{Q} \vec{\nabla}_{\mathbf{\Upsilon}}^T V \tag{2}$$

where ϵ is a positive scalar and $\mathbf{Q}$ is a constant positive matrix. Premultiplying (2) by $\vec{\nabla}_{\mathbf{\Upsilon}} V$, we get:

$$\frac{d}{dt} V(\mathbf{\Upsilon}) = -\epsilon \vec{\nabla}_{\mathbf{\Upsilon}} V \mathbf{Q} \vec{\nabla}_{\mathbf{\Upsilon}}^T V \le 0 \tag{3}$$

Thus V decreases with time as long as $\vec{\nabla}_{\mathbf{\Upsilon}} V \ne 0$, and remains constant when $\vec{\nabla}_{\mathbf{\Upsilon}} V = 0$. A common and simple choice for $\mathbf{Q}$ is the identity matrix $\mathbf{I}$. In this case, $\mathbf{\Upsilon}$ moves in the direction opposite to the gradient at $\mathbf{\Upsilon}$. This strategy is adopted in the classical approach described previously, where $\mathbf{F} = -\vec{\nabla}_{\mathbf{\Upsilon}}^T V$. Consider now a potential field $V_{\mathbf{f}} = V(\mathbf{f}(\mathbf{\Upsilon}))$ where $\mathbf{f}$ is differentiable everywhere in $\mathcal{W}$. The evolution equation of $\mathbf{f}$, when $\mathbf{\Upsilon}$ moves according to (2), is given by:

$$\dot{\mathbf{f}} = -\epsilon \left(\frac{\partial \mathbf{f}}{\partial \mathbf{\Upsilon}} \right) \mathbf{Q} \vec{\nabla}_{\mathbf{\Upsilon}}^T V = -\epsilon \left(\frac{\partial \mathbf{f}}{\partial \mathbf{\Upsilon}} \right) \mathbf{Q} \left(\frac{\partial \mathbf{f}}{\partial \mathbf{\Upsilon}} \right)^T \vec{\nabla}_{\mathbf{f}}^T V \tag{4}$$

In order that $\mathbf{f}$ moves in the direction opposite to the gradient of V at $\mathbf{f}$, the matrix $\mathbf{Q}$ can be chosen adequately:[2]

$$\mathbf{Q} = \mathbf{Q_f} = \left(\frac{\partial \mathbf{f}}{\partial \mathbf{\Upsilon}} \right)^+ \left(\frac{\partial \mathbf{f}}{\partial \mathbf{\Upsilon}} \right)^{+T} \tag{5}$$

---

[2]The matrix $\mathbf{A}^+$ denotes the pseudo-inverse of the matrix $\mathbf{A}$; it is the inverse matrix if $\mathbf{A}$ is a non-singular square matrix

Note that $\mathbf{Q}$ is a positive matrix and thus the relation (3) is verified. The evolution equation (4) can thus be rewritten:

$$\dot{\mathbf{f}} = -\epsilon \vec{\nabla}_{\mathbf{f}}^T V$$

The artificial force associated to the potential field $V_{\mathbf{f}}(\mathbf{f}(\mathbf{\Upsilon}))$ is thus:

$$\mathbf{F}_{\mathbf{f}}(\mathbf{\Upsilon}) = -\mathbf{Q}\vec{\nabla}_{\mathbf{\Upsilon}}^T V_{\mathbf{f}} = -\left(\frac{\partial \mathbf{f}}{\partial \mathbf{\Upsilon}}\right)^+ \vec{\nabla}_{\mathbf{f}}^T V_{\mathbf{f}} \tag{6}$$

When several potential functions are considered, the dominant artificial force derived from the potential $V_{\mathbf{f}}$ creates a dominant motion of $\mathbf{f}$ in the direction opposite to the gradient of $V_{\mathbf{f}}$ at $\mathbf{f}$. In practice, by using such process, it is more easy to control the relative influence of each force and thus to control the camera or the object trajectories.

In our case the control objective can be formulated as follow: to transfer the system to a desired point in the sensor space satisfying the following constraints:

1. the image trajectories correspond to a valid robot trajectory

2. all the considered image features remain in the camera field of view

3. the robot joint positions remain between their limits

To deal with the first constraint, the motion is firstly planned in the 3-D Cartesian space and then projected in the image space. The attractive potential ($V_{\mathbf{\Upsilon}}$) pulling the robot toward the goal configuration ($\mathbf{\Upsilon}_*$) is thus defined in the 3D-Cartesian space. The second and the third constraints are introduced through a repulsive potential $V_{\mathbf{s}}$ defined in the image and a repulsive potential $V_{\mathbf{q}}$ defined in the joint space. The total force is given by:

$$\mathbf{F} = \mathbf{F}_{\mathbf{\Upsilon}} + \gamma \mathbf{F}_{\mathbf{s}} + \chi \mathbf{F}_{\mathbf{q}} \tag{7}$$

where the scaling factors γ and χ allow us to adjust the relative influence of the different forces and can thus be used to take out of potential local minima. If a local minimum is reached, a motion is executed to take out of it by favoring the repulsive force. According to (6), the artificial forces can be written as follow:

$$\begin{cases} \mathbf{F}_{\mathbf{\Upsilon}} = -\left(\frac{\partial \mathbf{\Upsilon}}{\partial \mathbf{\Upsilon}}\right)^+ \vec{\nabla}_{\mathbf{\Upsilon}}^T V_{\mathbf{\Upsilon}} & = & -\vec{\nabla}_{\mathbf{\Upsilon}}^T V_{\mathbf{\Upsilon}} \\[2ex] \mathbf{F}_{\mathbf{s}} = -\left(\frac{\partial \mathbf{s}}{\partial \mathbf{r}}\frac{\partial \mathbf{r}}{\partial \mathbf{\Upsilon}}\right)^+ \vec{\nabla}_{\mathbf{s}}^T V_{\mathbf{s}} & = & -\mathbf{M}^+ \mathbf{L}^+ \vec{\nabla}_{\mathbf{s}}^T V_{\mathbf{s}} \\[2ex] \mathbf{F}_{\mathbf{q}} = -\left(\frac{\partial \mathbf{q}}{\partial \mathbf{r}}\frac{\partial \mathbf{r}}{\partial \mathbf{\Upsilon}}\right)^+ \vec{\nabla}_{\mathbf{q}}^T V_{\mathbf{q}} & = & -\mathbf{M}^+ \mathbf{J}(\mathbf{q})\vec{\nabla}_{\mathbf{q}}^T V_{\mathbf{q}} \end{cases} \tag{8}$$

where $\mathbf{M}$ is the Jacobian matrix that relates the variation of the camera velocity $\mathbf{T}_c$ to the variation of the chosen parameterization $\mathbf{\Upsilon}$: $\mathbf{T}_c = \mathbf{M}\dot{\mathbf{\Upsilon}}$. The form of the matrix $\mathbf{M}$ will be given in the sequel for the chosen workspace parameterizations. The matrix $\mathbf{J}(\mathbf{q})$ denotes the robot Jacobian and $\mathbf{L}$ is the interaction matrix related to $\mathbf{s}$ (also called image Jacobian).

It links the variation of the visual features with respect to the camera velocity $\mathbf{T}_c$: $\dot{\mathbf{s}} = \mathbf{L}\mathbf{T}_c$. For a point $\mathcal{M}^j$ with coordinates $[X^j\,Y^j\,Z^j]^T$ in the current camera frame and coordinates $\mathbf{p}^j = [u^j\,v^j\,1]^T$ (and $[x_j\,y_j\,1]^T = \mathbf{A}^{-1}\mathbf{p}^j$), the interaction matrix related to $\mathbf{s} = [u^j\,v^j]^T$ is given by:

$$\mathbf{L}(\mathbf{p}^j, Z^j) = \mathbf{a} \left[\begin{array}{cccccc} -\dfrac{1}{Z^j} & 0 & \dfrac{x^j}{Z^j} & x^j y^j & -(1 + x^{j^2}) & y^j \\[2mm] 0 & -\dfrac{1}{Z^j} & \dfrac{y^j}{Z^j} & (1 + y^{j^2}) & -x^j y^j & -x^j \end{array}\right]$$

where:

$$\mathbf{a} = \left[\begin{array}{cc} \alpha_u & \alpha_{uv} \\ 0 & \alpha_v \end{array}\right]$$

When $\mathbf{s}$ is composed of the image coordinates of n points, the corresponding interaction matrix is:

$$\mathbf{L}(\mathbf{s}, \mathbf{Z}) = \left[\mathbf{L}^T(p^1, Z^1)\cdots\mathbf{L}^T(p^n, Z^n)\right]^T$$

3 Path planning for a known target

In this part, the calibration parameters and the 3-D model of the target are supposed to be perfectly known. Knowing the coordinates $\mathbf{M}_o^j$, expressed in $\mathcal{F}_o$, of at least four points $\mathcal{M}^j$, it is possible from their projection to compute the initial and desired poses with respect to $\mathcal{F}_o$ [4], [11], that is the rotation matrix ${}^i\mathbf{R}_o$ (resp. ${}^*\mathbf{R}_o$) and the translation vector ${}^i\mathbf{t}_o$ (resp. ${}^*\mathbf{t}_o$) between $\mathcal{F}_i$ and $\mathcal{F}_o$ (resp. between $\mathcal{F}_*$ and $\mathcal{F}_o$).

3.1 Camera trajectory in the 3-D Cartesian space

Let ${}^*\mathbf{R}_k$ and ${}^*\mathbf{t}_k$ be the rotational matrix and the translational vector between $\mathcal{F}_k$ and $\mathcal{F}_*$ (see Figure 2). Let $\mathbf{u}_k$ and θ_k be the axis and the rotation angle obtained from ${}^*\mathbf{R}_k$. We choose $\boldsymbol{\Upsilon}_k = [{}^*\mathbf{t}_k^T\,(\mathbf{u}\theta)_k^T]^T$ as a parameterization of the workspace. We thus have $\boldsymbol{\Upsilon}_i = [{}^*\mathbf{t}_i^T\,(\mathbf{u}\theta)_i^T]^T$ and $\boldsymbol{\Upsilon}_* = \mathbf{0}_{1\times 6}$. The initial camera position $\boldsymbol{\Upsilon}_i$ is obtained from ${}^*\mathbf{t}_i$ and ${}^*\mathbf{R}_i$:

$$\begin{cases} {}^*\mathbf{R}_i & = {}^*\mathbf{R}_o\,{}^i\mathbf{R}_o^T \\[2mm] {}^*\mathbf{t}_i & = -\,{}^*\mathbf{R}_i\,{}^i\mathbf{t}_o + {}^*\mathbf{t}_o \end{cases}$$

According to the transition equation (1), where the attractive and the repulsive forces will be given in the subsection 3.4 and 3.5 respectively, we construct a path $\tau = \{\boldsymbol{\Upsilon}_k\,/\,k \in 1\cdots N\}$ as the sequence of successive path segments starting at the initial configuration $\boldsymbol{\Upsilon}_i$. Furthermore, the Z^j-coordinate in $\mathcal{F}_k$ of each point $\mathcal{M}^j$, which will be used in the repulsive force and in the control law, can be easily obtained at each iteration since:

$$\widetilde{\mathbf{M}}_k^j = [X_k^j\,Y_k^j\,Z_k^j]^T = \left[\begin{array}{cc} {}^*\mathbf{R}_k^T\,{}^*\mathbf{R}_o & {}^*\mathbf{R}_k({}^*\mathbf{t}_o - {}^*\mathbf{t}_k) \end{array}\right]\mathbf{M}_o^j$$
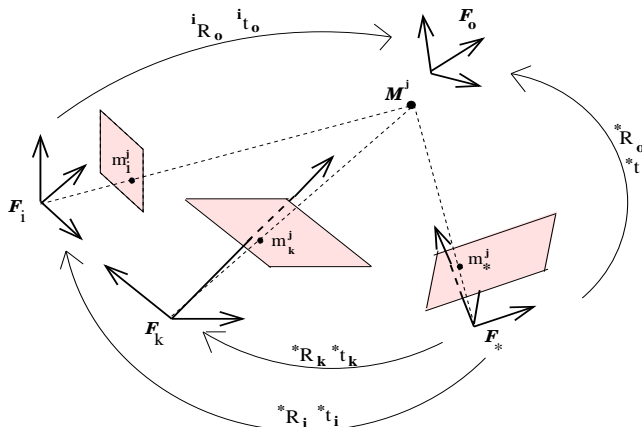
Figure 2: Computing intermediate views of the target points

A complete camera path in the 3-D Cartesian space is obtained as the sequence τ of N intermediate camera poses. A position-based control could thus be used to track it. However, it is more interesting to perform features trajectories in the image. Indeed, we thus exploit as well as possible the local stability and robustness of image-based servoing. Furthermore, it avoids the computation of the camera pose at each iteration of the servoing process.

3.2 Object trajectory in the image space

To perform image-based control, we build the trajectory of the projection $\mathbf{p}^j$ of each point $\mathcal{M}^j$ onto the image using the known coordinates $\mathbf{M}_o^j$ of $\mathcal{M}^j$ in $\mathcal{F}_o$. The trajectory in the image is obtained using the classical assumption that the camera performs a perfect perspective transformation with respect to the camera optical center (pinhole model):

$$r_k^j \mathbf{p}_k^j = [r_k^j u_k^j \ r_k^j v_k^j \ r_k^j]^T = \mathbf{A}[^k\mathbf{R}_o \ ^k\mathbf{t}_o]\mathbf{M}_o^j \tag{9}$$

$\mathbf{p}_k^j$ is easily obtained from (9) by dividing $r_k^j \mathbf{p}_k^j$ by its last component.

3.3 Trajectories in the joint space

To anticipate the possible encounter of a joint limit and to avoid it, we have to estimate the trajectory of the robot in the joint space. Indeed, the measure of the current joint coordinates is used in the computation of the repulsive potential related to the joint limits avoidance. If the manipulator position in the joint space is represented by $\mathbf{q} = [q^1 \cdots q^m]^T$, we have:

$$\frac{\partial \mathbf{q}}{\partial \mathbf{\Upsilon}} = \frac{\partial \mathbf{q}}{\partial \mathbf{r}} \frac{\partial \mathbf{r}}{\partial \mathbf{\Upsilon}} = \mathbf{J}^+(\mathbf{q})\mathbf{M} \tag{10}$$

$\mathbf{M}$ is the 6×6 Jacobian matrix that relates the variation of the camera velocity $\mathbf{T}_c$ to the variation of $\mathbf{\Upsilon}$:

$$\mathbf{M} = \left[\begin{array}{cc} {}^*\mathbf{R}_k^T & \mathbf{0}_{3 \times 3} \\ \mathbf{0}_{3 \times 3} & \mathbf{L}_{wk}^+ \end{array} \right]$$

The computation of $\mathbf{L}_{wk}^+$ can be found in [13]:[3]

$$\mathbf{L}_{wk}^+ = \mathbf{I}_{3 \times 3} + \frac{\theta_k}{2}\text{sinc}^2\left(\frac{\theta_k}{2}\right)[\mathbf{u}_k]_\wedge + (1 - \text{sinc}(\theta_k))[\mathbf{u}_k]_\wedge^2$$

The trajectory of the robot coordinates in the joint space is then obtained from the trajectory of $\mathbf{\Upsilon}$ by a linearization of (10) around $\mathbf{q}_k$:

$$\mathbf{q}_{k+1} = \mathbf{q}_k + \mathbf{J}^+(\mathbf{q}_k)\,\mathbf{M}\,(\mathbf{\Upsilon}_{k+1} - \mathbf{\Upsilon}_k)$$

In the next subsections, we present how the potential functions and the induced forces are defined and calculated.

3.4 Attractive potential and force

The attractive potential field $V_{\mathbf{\Upsilon}}$ is simply defined as a parabolic function in order to minimize the distance between the current position and the desired one:

$$V_{\mathbf{\Upsilon}}(\mathbf{\Upsilon}) = \frac{1}{2}\|\mathbf{\Upsilon} - \mathbf{\Upsilon}_*\|^2 = \frac{1}{2}\|\mathbf{\Upsilon}\|^2$$

The function $V_{\mathbf{\Upsilon}}$ is positive or null and attains its minimum at $\mathbf{\Upsilon}_*$ where $V_{\mathbf{\Upsilon}}(\mathbf{\Upsilon}_*) = 0$. It generates a force $\mathbf{F}_{\mathbf{\Upsilon}}$ that converges linearly towards the goal configuration (see (8)):

$$\mathbf{F}_{\mathbf{\Upsilon}}(\mathbf{\Upsilon}) = -\vec{\nabla}_{\mathbf{\Upsilon}}^T V_{\mathbf{\Upsilon}} = -\mathbf{\Upsilon} \tag{11}$$

When the repulsive potentials are not needed, the transition equation can be written (refer to (1) and (11)):

$$\mathbf{\Upsilon}_{k+1} = \left(1 - \frac{\varepsilon_k}{\|\mathbf{\Upsilon}_k\|}\right)\mathbf{\Upsilon}_k$$

Thus, $\mathbf{\Upsilon}_k$ is lying on the straight line passing by $\mathbf{\Upsilon}_i$ and $\mathbf{\Upsilon}_*$. As a consequence, the translation performed by the camera is a real straight line since $\mathbf{\Upsilon}_k$ is defined with respect to a motionless frame (that is $\mathcal{F}_*$). However, the object can get out of the camera field of view and the robot can attain its joint limits along this trajectory. To avoid this potential problems, two repulsive forces are introduced by deviating the camera trajectory when needed.

---

[3]$[\mathbf{u}]_\wedge$ denotes the skew symmetric matrix associated to the vector $\mathbf{u}$

3.5   Mechanical and visibility constraints

A. Joint limits avoidance.   The robot configuration $\mathbf{q}$ is called acceptable if each of its components is sufficiently far away from its corresponding joints limits. That is, $\mathbf{q}$ is acceptable if for all j, $q^j \in [q^j_{min} + l^j; \quad q^j_{max} - l^j]$, q^j_{min} and q^j_{max} being the minimum and the maximum allowable joint values for the jth joint and l^j being the distance of influence of the jth joint limit. We denote $\mathcal{L}$ the subset of the joint space of acceptable configurations. The repulsive potential $V_{\mathbf{q}}$ is defined as (see Figure 3):

$$
V_{\mathbf{q}}(\mathbf{q}) = \begin{cases} -v_q^2 \log \left(\prod_{j=1}^{m} (1 - \dfrac{q^j}{q^j_{max}})(1 - \dfrac{q^j}{q^j_{min}}) \right) & \text{if } \mathbf{q} \notin \mathcal{L} \\ \\ 0 & \text{if } \mathbf{q} \in \mathcal{L} \end{cases} \tag{12}
$$

In order to obtain a continuous and derivable potential field $V_{\mathbf{q}}$, v_q is chosen as a bounded function with null value in the boundary of $\mathcal{L}$:

$$
v_q(\mathbf{q}) = \prod_{j=1}^{n} (q^j - q^{lj}_{max})(q^j - q^{lj}_{min})
$$

where $q^{lj}_{min} = q^j_{min} + l^j$ and $q^{lj}_{max} = q^j_{max} - l^j$. The potential $V_{\mathbf{q}}$ is positive or null, tends to infinity as $\mathbf{q}$ gets closer to a joint limit, and it is null when the distance between $\mathbf{q}$ and the robot mechanical limits is more than l^j. The artificial repulsive force deriving from $V_{\mathbf{q}}$ is (refer to (8)):

$$
\mathbf{F_q} = -\mathbf{M}^+ \mathbf{J} \vec{\nabla}^T_{\mathbf{q}} V_{\mathbf{q}}
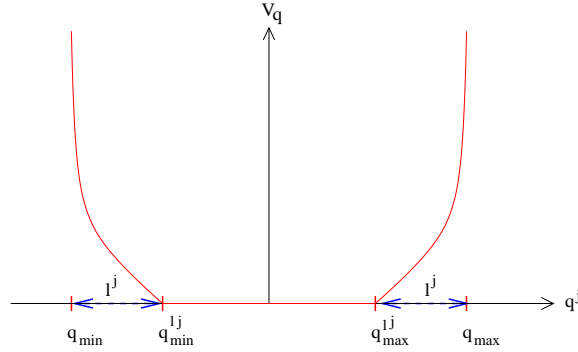$$

Figure 3: Repulsive potential for joints limits avoidance

where:

$$
\vec{\nabla}_{\mathbf{q}}^T V_{\mathbf{q}} = \begin{cases} 2 \begin{bmatrix} \nabla v_q^1 \\ \vdots \\ \nabla v_q^i \\ \vdots \\ \nabla v_q^m \end{bmatrix} v_q \phi_{\mathbf{q}} + v_q^2 \begin{bmatrix} -\frac{1}{q_{max}^1}(1 - \frac{q^1}{q_{max}^1})^{-1} - \frac{1}{q_{min}^1}(1 - \frac{q^1}{q_{min}^1})^{-1} \\ \vdots \\ -\frac{1}{q_{max}^i}(1 - \frac{q^i}{q_{max}^i})^{-1} - \frac{1}{q_{min}^i}(1 - \frac{q^i}{q_{min}^i})^{-1} \\ \vdots \\ -\frac{1}{q_{max}^m}(1 - \frac{q^m}{q_{max}^m})^{-1} - \frac{1}{q_{min}^m}(1 - \frac{q^m}{q_{min}^m})^{-1} \end{bmatrix} & \text{if } \mathbf{q} \notin \mathcal{L} \\[30pt] 0 & \text{if } \mathbf{q} \in \mathcal{L} \end{cases}
$$

with

$$
\begin{cases} \phi_{\mathbf{q}} = \log\left(\prod_{j=1}^{m} (1 - \frac{q^j}{q_{max}^j})(1 - \frac{q^j}{q_{min}^j}) \right) \\[20pt] \nabla v_q^i = (2q^i - q_{max}^{li} - q_{min}^{li}) \prod_{\substack{j=1 \\ j \neq i}}^{m} (q^j - q_{max}^{lj})(q^j - q_{min}^{lj}) \end{cases}
$$

B. Visibility constraint. A point $\mathcal{M}^j$, which projects onto the image plane at a point with image coordinates $\mathbf{p}^j = [u^j \, v^j \, 1]^T$, is known as visible if $u_j \in [u_m \, u_M]$ and $v_j \in [v_m \, v_M]$, where u_m, u_M, v_m, v_M are the limits of the image. The vector of image features $\mathbf{s}$ is called acceptable if for all $j \in \{1 \cdots n\}$, $u^j \in [u_m + \alpha; \, u_M - \alpha]$ and $v^j \in [v_m + \alpha; \, v_M - \alpha]$, where α is a positive constant denoting the distance of influence of the image boundary (see Figure 4(a)). We denote $\mathcal{C}$ the set of acceptable image features. One way to create a potential barrier around the camera field of view, ensuring that all features are always visible and do not affect the camera motion when they are sufficiently far enough from the image limits, is to define the repulsive potential $V_{\mathbf{s}}(\mathbf{s})$ as (see Figure 4(b)) :

$$
V_{\mathbf{s}}(\mathbf{s}) = \begin{cases} -v_s^2 \log\left(\prod_{j=1}^{n} (1 - \frac{u^j}{u_M})(1 - \frac{u^j}{u_m})(1 - \frac{v^j}{v_M})(1 - \frac{v^j}{v_m}) \right) & \text{if } \mathbf{s} \notin \mathcal{C} \\[20pt] 0 & \text{if } \mathbf{s} \in \mathcal{C} \end{cases} \tag{13}
$$

As for the previous potential function, v_s is chosen as a bounded function with null value in the boundary of $\mathcal{C}$:

$$
v_s(\mathbf{s}) = \prod_{j=1}^{n} (u^j - u_M^\alpha)(u^j - u_m^\alpha)(v^j - v_M^\alpha)(v^j - v_m^\alpha)
$$

where $u_m^\alpha = u_m + \alpha$, $u_M^\alpha = u_M - \alpha$, $v_m^\alpha = v_m + \alpha$ and $v_M^\alpha = v_M - \alpha$.
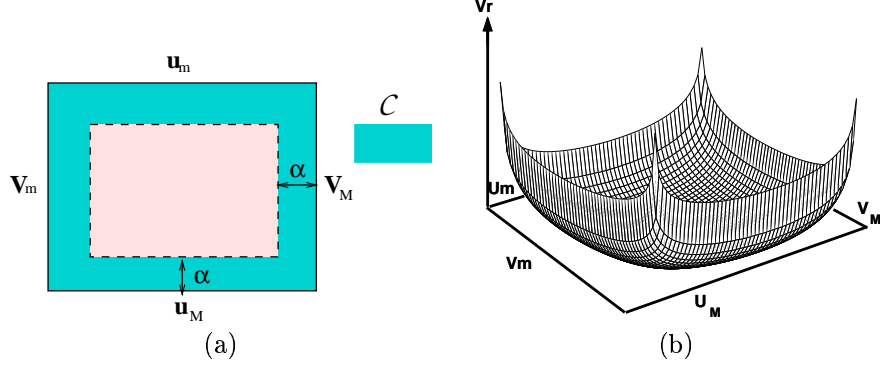

Figure 4: (a) Image limits, (b) Repulsive potential for visibility constraint

The function $V_{\mathbf{s}}$ is positive or null, tends to infinity when at less one selected image features gets closer to the image limits, and it is null when all image features are sufficiently far away from the image limits. The artificial repulsive force deriving from $V_{\mathbf{s}}$ is:

$$\mathbf{F_s}(\boldsymbol{\Upsilon}) = -\mathbf{M}^+\mathbf{L}^+\vec{\nabla}_{\mathbf{s}}^T V_{\mathbf{s}} \tag{14}$$

where $\vec{\nabla}_{\mathbf{s}}^T V_{\mathbf{s}}$ is easily obtained from (13):

$$\vec{\nabla}_{\mathbf{s}}^T V_{\mathbf{s}} = \begin{cases} 2 \begin{bmatrix} \nabla v_s^0 \\ \vdots \\ \nabla v_s^{2i} \\ \nabla v_s^{2i+1} \\ \vdots \\ \nabla v_s^{2n-1} \end{bmatrix} v_s \psi_{\mathbf{s}} + v_s^2 \begin{bmatrix} -\frac{1}{u_M}(1-\frac{u^1}{u_M})^{-1} - \frac{1}{u_m}(1-\frac{u^1}{u_m})^{-1} \\ \vdots \\ -\frac{1}{v_M}(1-\frac{v^i}{v_M})^{-1} - \frac{1}{v_m}(1-\frac{v^i}{v_m})^{-1} \\ -\frac{1}{u_M}(1-\frac{u^i}{u_M})^{-1} - \frac{1}{u_m}(1-\frac{u^i}{u_m})^{-1} \\ \vdots \\ -\frac{1}{v_M}(1-\frac{v^n}{v_M})^{-1} - \frac{1}{v_m}(1-\frac{v^n}{v_m})^{-1} \end{bmatrix} & \text{if } \mathbf{s} \notin \mathcal{C} \\[6pt] 0 & \text{if } \mathbf{s} \in \mathcal{C} \end{cases}$$

with

$$
\begin{cases}
\psi_{\mathbf{s}} = \log\left(\prod_{j=1}^{n}\left((1-\tfrac{u^j}{u_M})(1-\tfrac{u^j}{u_m})(1-\tfrac{v^j}{v_M})(1-\tfrac{v^j}{v_m})\right)\right) \\[1.5em]
\nabla v_s^{2i} = (2u^i - u_M^\alpha - u_m^\alpha)(v^i - v_M^\alpha)(v^i - v_m^\alpha) \prod_{\substack{j=1 \\ j \neq i}}^{n} (u^j - u_M^\alpha)(u^j - u_m^\alpha)(v^j - v_M^\alpha)(v^j - v_m^\alpha) \\[1.5em]
\nabla v_s^{2i+1} = (2v^i - v_M^\alpha - v_m^\alpha)(u^i - u_M^\alpha)(u^i - u_m^\alpha) \prod_{\substack{j=1 \\ j \neq i}}^{n} (u^j - u_M^\alpha)(u^j - u_m^\alpha)(v^j - v_M^\alpha)(v^j - v_m^\alpha)
\end{cases}
$$

3.6   Summary

By using a target model and a calibrated camera, the trajectory of a set of n points in the image has been obtained as a sequence of N vectors $\mathcal{S} = \{\mathbf{s}_k / k \in 1 \cdots N\}$. A block diagram of the path planning scheme is given in Figure 5. The obtained trajectory provides some good expected properties: along this trajectory the target remains in the camera field of view, the corresponding robot motion is physically realizable and the camera trajectory is a straight line outside the area where the repulsives forces are needed. The set $\mathcal{Z} = \{\mathbf{Z}_k = [Z_1 \cdots Z_n]/k \in 1 \cdots N\}$, which will be used in the control law, has been also determined.

In the next part, we extend this method to the case where the object shape and dimensions are unknown and where the calibration is well or badly estimated.
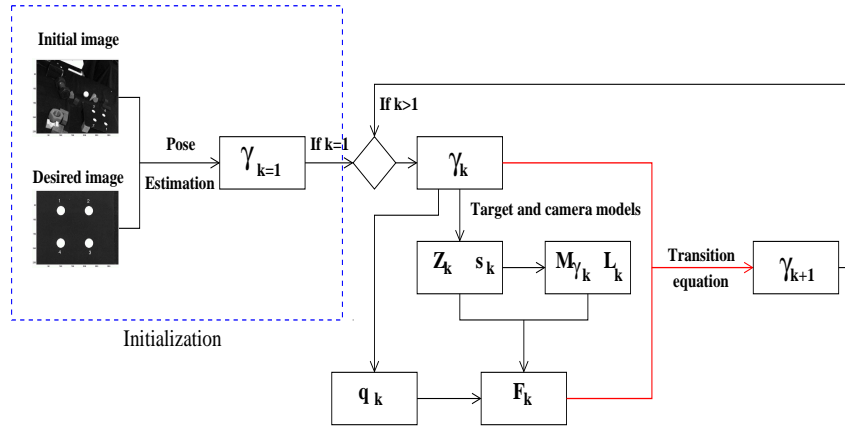

Figure 5: Block diagram of the path planning for a known object

4 Path planning for an unknown target

In this section, we consider that the target model is not available. In this case the camera pose can not be estimated. Only a scaled Euclidean reconstruction can be obtained by performing a partial pose estimation as described in the next subsection. This partial pose estimation and the relations linking two views of a static object are then exploited to design a path of the object in the image space. First, we present the method with accurate calibration parameters and then, the robustness with respect to modeling errors is studied. For conveniance, the rotation matrix $^*\mathbf{R}_k$ and the translation vector $^*\mathbf{t}_k$ are denoted $\mathbf{R}_k$ and $\mathbf{t}_k$ in the sequel.

4.1 Scaled Euclidean reconstruction

Consider a 3-D reference plane Π given in the desired camera frame $\mathcal{F}_*$ by the vector $\pi^T = [\mathbf{n}^* - d^*]$, where $\mathbf{n}^*$ is its unitary normal in $\mathcal{F}_*$ and d^* is the distance from Π to the origin of $\mathcal{F}_*$ (see Figure 6). It is well known that there is a projective homography matrix $\mathbf{G}_k$, relating the image points in the current and the desired images, such that [5]:

$$\alpha_k^j \mathbf{p}_k^j = \mathbf{G}_k \mathbf{p}_*^j + \beta^j \mathbf{e}_k \quad \text{with} \quad \mathbf{e}_k = -\mathbf{A}\mathbf{R}_k^T \mathbf{t}_k \tag{15}$$

where α_k^j is a positive scaling factor and β^j is a constant scaling factor null if the target point belongs to Π. More precisely, if we define the signed distance $d(\mathcal{M}^j, \Pi) = \pi \, \mathbf{M}_*^j$, we have:

$$\beta^j = -\frac{d(\mathcal{M}^j, \Pi)}{Z_*^j d^*} \tag{16}$$

Given at least four matched points belonging to Π, $\mathbf{G}_k$ can be estimated by solving a linear system. If the plane Π is defined by 3 points, at least five supplementary points are necessary to estimate the homography matrix by using for example the linear algorithm proposed in [12]. Assuming that the camera calibration is known, the Euclidean homography $\mathbf{H}_k$ of plane Π is estimated as follow:

$$\mathbf{H}_k = \mathbf{A}^+ \mathbf{G}_k \mathbf{A} \tag{17}$$

and it can be decomposed into a rotation matrix and a rank 1 matrix [5]:

$$\mathbf{H}_k = \mathbf{R}_k^T - \mathbf{R}_k^T \mathbf{t}_{dk} \mathbf{n}^{*T} \quad \text{where} \quad \mathbf{t}_{dk} = \frac{\mathbf{t}_k}{d^*} \tag{18}$$

From $\mathbf{H}_k$, it is thus possible to determine the camera motion parameters (that is the rotation $\mathbf{R}_k$ and the scaled translation $\mathbf{t}_{dk}$) and the structure of the observed scene (for example the vector $\mathbf{n}^*$) [5]. The ratio $\rho_k^j = Z_k^j/d^*$ can easily be estimated [13]:

$$\begin{cases} \rho_k^j = \dfrac{Z_k^j}{d^*} = \dfrac{1 - \mathbf{n}^{*T} \mathbf{R}_k^{2T} \mathbf{t}_{dk}}{\mathbf{n}^{*T} \mathbf{R}_k \mathbf{m}_k^j} & \text{if} \quad \mathcal{M}^j \in \Pi \\[4mm] \rho_k^j = \dfrac{Z_k^j}{d^*} = \sigma_k^j \dfrac{\|\mathbf{R}_k^T \mathbf{t}_{dk}\|}{\|\sigma_k^j \mathbf{m}_k^j - \mathbf{R}_k^T \mathbf{m}_*^j\|} & \text{if} \quad \mathcal{M}^j \notin \Pi \end{cases} \tag{19}$$

where $\sigma_k^j = \frac{\|[\mathbf{R}_k^T \mathbf{t}_{dk}]_\wedge \mathbf{R}_k^T \mathbf{m}_*^j\|}{\|[\mathbf{R}_k^T \mathbf{t}_{dk}]_\wedge \mathbf{m}_k^j\|}$. These parameters are important since they are used in the path planning generator and in the control scheme.
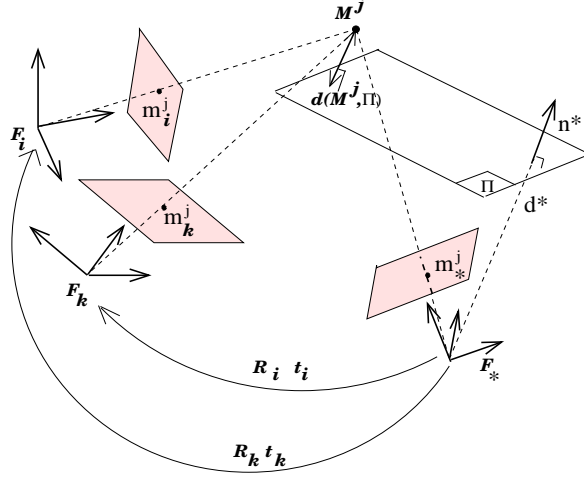

Figure 6: Scaled 3-D Cartesian trajectory

4.2 Scaled 3-D Cartesian trajectory

We now choose $\boldsymbol{\Upsilon}_k = [\mathbf{t}_{dk}^T \ (\mathbf{u}\theta)_k^T]^T$ as parameterization of the workspace, since $\mathbf{t}_{dk}$ is available while $\mathbf{t}_k$ is not. We thus have $\boldsymbol{\Upsilon}_i^T = [\mathbf{t}_{di}^T \ (\mathbf{u}\theta)_i^T]$ and $\boldsymbol{\Upsilon}_* = \mathbf{0}_{6\times 1}$. From initial and desired images, it is possible to compute the homography $\mathbf{H}_i$ and then to obtain $\mathbf{R}_i$, $\mathbf{t}_{di}$, $\mathbf{n}^*$ and thus $\boldsymbol{\Upsilon}_i$. As in the previous section, we construct a path τ starting at $\boldsymbol{\Upsilon}_i$ and oriented along the induced forces given in this case by:

$$\begin{cases} \mathbf{F}_{\boldsymbol{\Upsilon}}(\boldsymbol{\Upsilon}) &= -\boldsymbol{\Upsilon} \\[2mm] \mathbf{F}_{\mathbf{s}}(\boldsymbol{\Upsilon}) &= -\mathbf{M}^+\mathbf{L}^+\vec{\nabla}_{\mathbf{s}}^T V_{\mathbf{s}} \\[2mm] \mathbf{F}_{\mathbf{q}}(\boldsymbol{\Upsilon}) &= -\mathbf{M}^+\mathbf{J}\vec{\nabla}_{\mathbf{q}}^T V_{\mathbf{q}} \end{cases}$$

The Jacobian matrix of parameterization $\mathbf{M}(d^*)$ is now given by:

$$\mathbf{M}(d^*) = \begin{bmatrix} d^*\mathbf{R}_k^T & \mathbf{0}_{3\times 3} \\ \mathbf{0}_{3\times 3} & \mathbf{L}_{wk}^+ \end{bmatrix} \tag{20}$$

Note that $\mathbf{M}$ now depends of the unknown parameter d^*. However, as shown in the sequel, this parameter does not have any influence on the path planning process if only the visibility constraint is considered. Furthermore, the interaction matrix depends of the depth

vector $\mathbf{Z}$. Contrary to the previous case, it can not be computed directly from the scaled parameterization $\boldsymbol{\Upsilon}$. But the ratio $\rho_k^j = Z_k^j/d^*$ can easily be estimated from the scaled parameterization and the image features according to (19). Thus we rewrite the interaction matrix $\mathbf{L}(\mathbf{s}, \mathbf{Z})$ as follow:

$$\mathbf{L}(\mathbf{s}, \boldsymbol{\Gamma}, d^*) = \left[\begin{array}{cc} \frac{1}{d^*}\mathbf{S} & \mathbf{Q} \end{array} \right] \tag{21}$$

where $\boldsymbol{\Gamma} = \left[\rho_k^1 \cdots \rho_k^n \right]$, $\mathbf{S} = [\mathbf{S}^{1T} \cdots \mathbf{S}^{nT}]^T$ and $\mathbf{Q} = [\mathbf{Q}^{1T} \cdots \mathbf{Q}^{nT}]^T$ are two $2n \times 3$ matrices independent of d^*:

$$\begin{cases} \mathbf{S}^j & = & \mathbf{a} \left[\begin{array}{ccc} -\frac{1}{\rho_k^j} & 0 & \frac{x_k^j}{\rho_k^j} \\[2mm] 0 & -\frac{1}{\rho_k^j} & \frac{y_k^j}{\rho_k^j} \end{array} \right] \\[8mm] \mathbf{Q}^j & = & \mathbf{a} \left[\begin{array}{ccc} x_k^j y_k^j & -1 - x_k^{j\,2} & y_k^j \\[2mm] 1 + y_k^{j\,2} & -x_k^j y_k^j & -x_k^j \end{array} \right] \end{cases}$$

The partial pose of the camera $\boldsymbol{\Upsilon}_k$ is thus computed at each iteration. Then, $\mathbf{R}_k$ and $\mathbf{t}_{dk}$ are directly obtained from $\boldsymbol{\Upsilon}_k$. According to (19), the vector $\boldsymbol{\Gamma} = \left[\rho_k^1 \cdots \rho_k^n \right]$ is obtained from $\boldsymbol{\Upsilon}_k$. Note that in this case the path of the robot in the joint space is given by:

$$\mathbf{q}_{k+1} = \mathbf{q}_k + \mathbf{J}^+(\mathbf{q}_k)\, \mathbf{M}_k(d^*)\, (\boldsymbol{\Upsilon}_{k+1} - \boldsymbol{\Upsilon}_k)$$

Finally, the image features at iteration k are computed as described in the next subsection.

4.3   Object trajectory in the image space

The homography matrix $\mathbf{G}_k$ of plane Π relating the current and desired images can be computed from $\boldsymbol{\Upsilon}_k$ by using (17) and (18):

$$\mathbf{G}_k = \mathbf{A}(\mathbf{R}_k^T - \mathbf{R}_k^T \mathbf{t}_{dk} \mathbf{n}^{*T})\mathbf{A}^+ \tag{22}$$

According to (15) the image coordinates of the points $\mathcal{M}^j$ at time k are given by:

$$\mu_k^j \mathbf{p}_k^j = [\mu_k^j u_k^j \ \ \mu_k^j v_k^j \ \ \mu_k^j] = \mathbf{G}_k \mathbf{p}_*^j + \beta^j \mathbf{e}_k \tag{23}$$

where (refer to (15) and (16)):

$$\beta^j \mathbf{e}_k = \frac{d(\mathcal{M}^j, \Pi)}{Z_*^j d^*} \mathbf{A} \mathbf{R}_k^T \mathbf{t}_k = \frac{d(\mathcal{M}^j, \Pi)}{Z_*^j} \mathbf{A} \mathbf{R}_k^T \mathbf{t}_{dk}$$

Using the previous relation, (23) can be rewritten:

$$\mu_k^j \mathbf{p}_k^j = \mathbf{G}_k \mathbf{p}_*^j + \frac{d(\mathcal{M}^j, \Pi)}{Z_*^j} \mathbf{A} \mathbf{R}_k^T \mathbf{t}_{dk} \tag{24}$$

Furthermore, if the relation (24) is applied between the desired and the initial camera positions, we obtain easily [4]:

$$\frac{d(\mathcal{M}^j, \Pi)}{Z_*^j} = \text{sign} \left(\frac{\left(\mu_i^j \mathbf{p}_i^j - \mathbf{G}_i \mathbf{p}_*^j \right)_1}{(\mathbf{A}\mathbf{R}_i \mathbf{t}_{di})_1} \right) \frac{\|\mathbf{G}_i \mathbf{p}_*^j \wedge \mathbf{p}_i^j\|}{\|\mathbf{A}\mathbf{R}_i \mathbf{t}_{di} \wedge \mathbf{p}_i^j\|} \tag{25}$$

The relations (22), (24) and (25) allow to compute $\mu_k^j \mathbf{p}_k^j$ from $\mathbf{\Upsilon}_k$ and the initial and desired visual features. The image coordinates $\mathbf{p}_k^j$ are finally computed by dividing $\mu_k^j \mathbf{p}_k^j$ by its last component.

In the next subsections, we consider that the repulsive force related to the joint limit avoidance is not activated (i.e $\chi_k = 0$) and the effects of error on the intrinsic parameters and on the depth d^* are studied.

4.4 Influence of errors on d^*

If the joint limits avoidance is not considered, the parameter d^* appears only in repulsive force through the matrix $\mathbf{W}$ defined as the product of $\mathbf{M}^+(d^*)$ and $\mathbf{L}^+(\mathbf{s}, \mathbf{\Gamma}, d^*)$. However, according to (20) and (21), we have at time k:

$$\mathbf{W}(\mathbf{\Upsilon}_k, \mathbf{\Gamma}_k, \mathbf{s}_k) = (\mathbf{L}(\mathbf{s}_k, \mathbf{\Gamma}_k, d^*) \mathbf{M}_k(d^*))^+ = \left[\begin{array}{c} \mathbf{S}(\mathbf{s}_k, \mathbf{\Gamma}_k) \mathbf{R}_k^T \\ \mathbf{Q}(\mathbf{s}_k) \mathbf{L}_{wk}^+ \end{array} \right]^+$$

$\mathbf{W}$ is independent on the parameter d^*. Thus, the trajectories in the retinal space are also independent on d^* and are not affected by possible errors on d^*. Let us note that it is unfortunately not the case if joints limits avoidance is also considered.

4.5 Influence of errors on the intrinsic parameters

If the camera is not perfectly calibrated and $\widehat{\mathbf{A}}$ is used instead of $\mathbf{A}$, the estimated initial homography matrix $\widehat{\mathbf{H}}_i$ is:

$$\widehat{\mathbf{H}}_i = \widehat{\mathbf{A}}^+ \mathbf{A} \mathbf{H}_i \mathbf{A}^+ \widehat{\mathbf{A}} = \delta\mathbf{A} \mathbf{H}_i \delta\mathbf{A}^+ \tag{26}$$

where $\delta\mathbf{A} = \widehat{\mathbf{A}}^+ \mathbf{A}$. Let us make the following assumption:

$$\widehat{\mathbf{H}}_i = \delta\mathbf{A} \mathbf{H}_i \delta\mathbf{A}^+ \implies \widehat{\mathbf{H}}_k = \delta\mathbf{A} \mathbf{H}_k \delta\mathbf{A}^+ \tag{27}$$

It means that the initial error on the estimated homography is propagated along the trajectory and implies that the estimated homography at time k can be decomposed in the sum of a matrix similar to a rotation matrix and a rank 1 matrix:

$$\widehat{\mathbf{H}}_k = \widehat{\mathbf{H}}_{\infty k} - \widehat{\mathbf{T}}_k \widehat{\mathbf{n}}^{*T} \tag{28}$$

---

[4] $(\mathbf{v})_j$ is the jth components of $\mathbf{v}$ and $sign(b)$ denotes the "sign" of b.

where $\widehat{\mathbf{H}}_{\infty k} = \delta \mathbf{A} \mathbf{R}_k^T \delta \mathbf{A}^+$, $\widehat{\mathbf{n}}^{*T} = \frac{\mathbf{n}^{*T}\delta\mathbf{A}}{\|\mathbf{n}^{*T}\delta\mathbf{A}^+\|}$ and $\widehat{\mathbf{T}}_k = \|\mathbf{n}^{*T}\delta\mathbf{A}^+\|\delta\mathbf{A}\mathbf{T}_k$ with $\mathbf{T}_k = \mathbf{R}_k^T \mathbf{t}_{dk}$ [13]. Obviously, $\mathbf{G}_i$, $\mathbf{p}_*^j$ and $\mathbf{p}_i^j$ are not affected by errors on intrinsic parameters, since they are extracted or computed directly from image data. According to (24), (25) and (28), the obtained homogeneous image coordinates $\widehat{\mathbf{p}}_k^j$ in the presence of calibration errors are given by:

$$\widehat{\mu}_k^j \widehat{\mathbf{p}}_k^j = \widehat{\mathbf{A}}\widehat{\mathbf{H}}_k\widehat{\mathbf{A}}^+\mathbf{p}_*^j + sign\left(\frac{\left(\mu_i^j\mathbf{p}_i^j - \mathbf{G}_i\mathbf{p}_*^j\right)_1}{\left(\widehat{\mathbf{A}}\,\widehat{\mathbf{T}}_i\right)_1}\right)\frac{\|\mathbf{G}_i\mathbf{p}_*^j \wedge \mathbf{p}_i^j\|}{\|\widehat{\mathbf{A}}\widehat{\mathbf{T}}_i \wedge \mathbf{p}_i^j\|}\widehat{\mathbf{A}}\widehat{\mathbf{T}}_k \qquad (29)$$

Since $\widehat{\mathbf{A}}\widehat{\mathbf{T}}_k = \|\mathbf{n}^{*T}\delta\mathbf{A}^+\|\mathbf{A}\mathbf{T}_k$, we have the following equalities:

$$\begin{cases} sign\left(\dfrac{\left(\mu_i^j\mathbf{p}_i^j - \mathbf{G}_i\mathbf{p}_*^j\right)_1}{\left(\widehat{\mathbf{A}}\,\widehat{\mathbf{T}}_i\right)_1}\right) = sign\left(\dfrac{\left(\mu_i^j\mathbf{p}_i^j - \mathbf{G}_i\mathbf{p}_*^j\right)_1}{\left(\mathbf{A}\,\mathbf{T}_i\right)_1}\right) \\[3ex] \dfrac{\|\mathbf{G}_i\mathbf{p}_*^j \wedge \mathbf{p}_i^j\|}{\|\widehat{\mathbf{A}}\widehat{\mathbf{T}}_i \wedge \mathbf{p}_i^j\|}\widehat{\mathbf{A}}\,\widehat{\mathbf{T}}_k = \dfrac{\|\mathbf{G}_i\mathbf{p}_*^j \wedge \mathbf{p}_i^j\|}{\|\mathbf{A}\mathbf{T}_i \wedge \mathbf{p}_i^j\|}\mathbf{A}\mathbf{T}_k \end{cases} \qquad (30)$$

Furthermore, we also have:

$$\widehat{\mathbf{A}}\widehat{\mathbf{H}}_k\widehat{\mathbf{A}}^+ = \widehat{\mathbf{A}}\delta\mathbf{A}\mathbf{H}_k\delta\mathbf{A}^+\widehat{\mathbf{A}}^+ = \mathbf{A}\mathbf{H}_k\mathbf{A}^+ \qquad (31)$$

By injecting (30) and (31) in (29), we finally obtain:

$$\widehat{\mu}_k^j\widehat{\mathbf{p}}_k^j = \mu_k^j\mathbf{p}_k^j$$

Therefore, under assumption (27), the trajectories in the image are not disturbed by errors on intrinsic parameters. We will check this nice property on the experimental results given in Section 7.

4.6 Summary

In this part, trajectories of a set of n points in retinal space have been obtained as a sequence of N vectors $\mathcal{S} = \{\mathbf{s}_k/k \in 1\cdots N\}$ without any model of the scene. The set $\mathcal{R} = \{\mathbf{\Gamma}_k/k \in 1\cdots N\}$, which will be used in the control law, has been also computed. Moreover, we have seen that the planned path is independent of camera calibration if the joint limit avoidance constraint is not considered. A block diagram of the path planning is given in Figure 7.
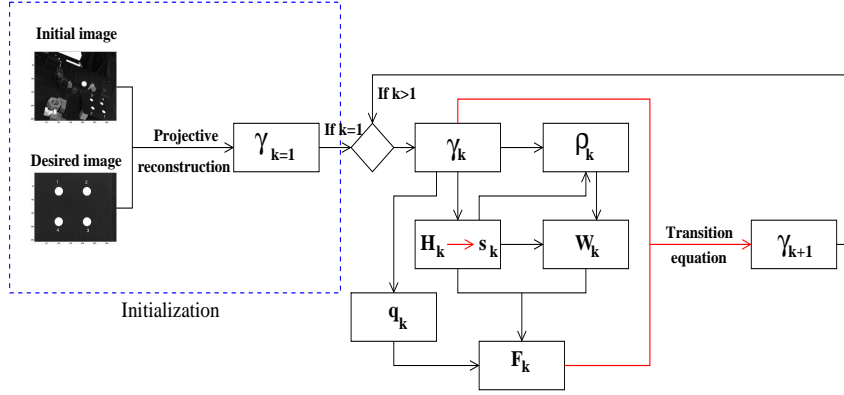
Figure 7: Block diagram of the path planning for an unknown object

5 Performing C^2 image trajectories

In the previous subsections, we have obtained discrete trajectories. In order to design continuous and derivable curves and thus to improve the dynamic behavior of the system, we use cubic B-spline interpolation. The spline interpolation problem is usually stated as: given data points $\mathcal{S} = \{\mathbf{s}_k / k \in 1 \cdots N\}$ and a set of parameter values $\mathcal{T} = \{t_k / k \in 1 \cdots N\}$, we want a cubic B-spline curve $\mathbf{s}(t)$ such that $\mathbf{s}(t_k) = \mathbf{s}_k$. In practice, parameter values are rarely given. In our case, we can adjust them to the distribution of the vector of image features $\mathbf{s}_k$ or using the distribution of the camera positions $\boldsymbol{\Upsilon}_k$. The distance between two successive camera positions $\boldsymbol{\Upsilon}_k$ and $\boldsymbol{\Upsilon}_{k+1}$ can be chosen constant by fixing ε_k at a constant value. Let us note that the distance in the image between a point at time k and $k + 1$ is not necessarily constant using a constant value for ε_k (see Figure 8). In order to control efficiently the camera velocity, the time values are chosen spacing proportionally to the distances between camera positions. Thus, the time between two consecutive frames is constant: $\Delta t_{k+1} = t_{k+1} - t_k = T$, where T can be chosen for example as the video rate.

Given the data vectors $\mathbf{s}_k$ and the parameters values t_k, the image data can be interpolated by using a natural cubic B-spline interpolation and we obtain a C^2 function $\mathbf{s}(t)$ defined for $(k - 1)T \le t \le kT$ by:

$$\mathbf{s}(t) = \mathbf{A}_k t^3 + \mathbf{B}_k t^2 + \mathbf{C}_k t + \mathbf{D}_k \tag{32}$$

where the $n \times n$ diagonal matrices $\mathbf{A}_k$, $\mathbf{B}_k$, $\mathbf{C}_k$, $\mathbf{D}_k$ are obtained from $\mathcal{S}$ and $\mathcal{T}$. The depth Z (resp. the ratio ρ) in the case of a known object (resp. in the case of an unknown object) appears in the control law. By using the same process, $\mathbf{Z}(t) = \left[Z^1(t) \cdots Z^n(t) \right]$ (resp. $\boldsymbol{\Gamma}(t) = \left[\rho^1(t) \cdots \rho^n(t) \right]$) is computed from $\mathcal{Z} = \{\mathbf{Z}_k / k \in 1 \cdots N\}$ and $\mathcal{T}$ (resp. from $\mathcal{R} = \{\boldsymbol{\Gamma}_k / k \in 1 \cdots N\}$ and $\mathcal{T}$).
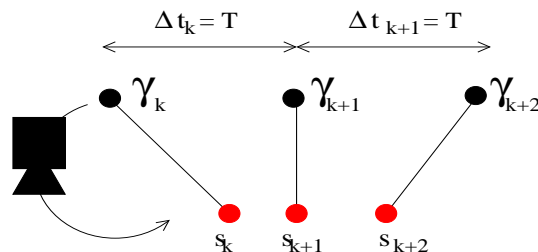
Figure 8: Controlling the time along the camera trajectory

6   Control scheme

To track the image trajectories using an image-based control scheme, we use the following vision-based task function $\mathbf{e}$ to be regulated to $\mathbf{0}$:

$$\mathbf{e} = \widehat{\mathbf{L}}^{+}(\mathbf{s}(\mathbf{r}(t)) - \mathbf{s}^{*}(t))$$

The time varying vector $\mathbf{s}^{*}(t)$ is the desired trajectory of $\mathbf{s}$ computed as previously explained and the matrix $\widehat{\mathbf{L}}^{+}$ is the pseudo-inverse of a chosen model of $\mathbf{L}$. The value of $\mathbf{L}$ at the current desired position is used for $\widehat{\mathbf{L}}$. More precisely:

- if the target is known $\widehat{\mathbf{L}} = \mathbf{L}(\mathbf{s}^{*}(t), \mathbf{Z}^{*}(t))$

- else $\widehat{\mathbf{L}} = \mathbf{L}(\mathbf{s}^{*}(t), \mathbf{\Gamma}^{*}(t), \widehat{d^{*}})$, $\widehat{d^{*}}$ being an estimated value of d^{*} (see (21)):

$$\mathbf{L}(\mathbf{s}^{*}(t), \mathbf{\Gamma}^{*}(t), \widehat{d^{*}}) = \left[\ \frac{1}{\widehat{d^{*}}}\mathbf{S}(\mathbf{s}^{*}(t), \mathbf{\Gamma}^{*}(t)) \quad \mathbf{Q}(\mathbf{s}^{*}(t)) \ \right]$$

The exponential decay of $\mathbf{e}$ toward $\mathbf{0}$ can be obtained by imposing $\dot{\mathbf{e}} = -\lambda\mathbf{e}$ (λ being a proportional gain), the corresponding control law is:

$$\mathbf{T}_{c} = -\lambda\mathbf{e} - \frac{\partial\mathbf{e}}{\partial t} \tag{33}$$

where $\mathbf{T}_{c}$ is the camera velocity sent to the robot controller. If the target is known to be motionless, we have $\frac{\partial\mathbf{e}}{\partial t} = -\widehat{\mathbf{L}}^{+}\frac{\partial\mathbf{s}^{*}}{\partial t}$ and the camera velocity can be rewritten:

$$\mathbf{T}_{c} = -\lambda\mathbf{e} + \widehat{\mathbf{L}}^{+}\frac{\partial\mathbf{s}^{*}}{\partial t}$$

where the term $\widehat{\mathbf{L}}^{+}\frac{\partial\mathbf{s}^{*}}{\partial t}$ allows to compensate the tracking error. More precisely, we have from (32):

$$\frac{\partial\mathbf{s}^{*}}{\partial t} = 3\mathbf{A}_{k}t^{2} + 2\mathbf{B}_{k}t + \mathbf{C}_{k} \quad \text{for} \quad (k-1)T \leq t \leq kT$$

As will be shown in the next section, this control law is robust with respect to modeling errors and noise perturbations since the error function used as input remains small and is directly computed from visual features.
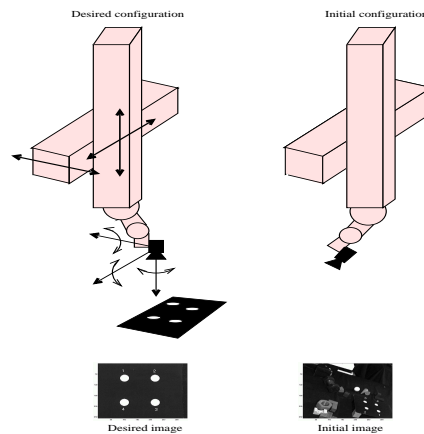
Figure 9: Experimental setup

7 Experimental results

The proposed methods have been tested on a six d-o-f eye-in-hand system. Since we were not interested in image processing issues in this paper, the target is composed by white marks (see Figure 9). The extracted visual features are the image coordinates of the center of gravity of each mark. This section is organized as follows. In Subsection 7.1, we present experiments which confirm that introducing a path planning step improves significantly the robustness with respect to modeling errors. In the Subsections 7.2, 7.3 and 7.4, only the repulsive potential associated to the visibility constraint is activated. The results obtained with a planar target and an unknown non-planar target are discussed. In Subsection 7.5, we comment experiments obtained when both joint limits avoidance and visibility constraints are taken into account.

7.1 General interest for path planning

We first show that it is, in general, more interesting to plan the image trajectory $\mathbf{s}^*(t)$ we want to achieve rather than to use a constant reference $\mathbf{s}^*$. To achieve an exponential decay of the sensor signal from its initial value $\mathbf{s}_i$ to its desired one $\mathbf{s}^*$ we can use the following classical control law:

$$\mathbf{T}_c = -\lambda \widehat{\mathbf{L}}^+ (\mathbf{s}(t) - \mathbf{s}^*)$$

where $\widehat{\mathbf{L}} = \mathbf{L}(\mathbf{s}(t), \mathbf{Z}(t))$. With this scheme, we expect that each point moves in the image according to a straight line, even if we know that it is not possible in all cases [1]. In order to check the robustness with respect to modeling errors, we carried out three experiments:

1) the correct intrinsic parameters are used. The reference $\mathbf{s}^*$ has been taken constant.

2) An error of 40% is introduced on the intrinsic parameters. As in the previous case, the reference $\mathbf{s}^*$ has been taken constant.

3) The same error of 40% is introduced on the intrinsic parameters. A variable reference $\mathbf{s}^*(t)$ is used such that the expected trajectories are straight lines in the image. Let us recall that such trajectories are not always physically valid [1]. Such simple planning approach can thus not be generalized. In this experiment, we have chosen a particular and valid configuration such that the realized trajectories are the same for both control schemes when correct calibration is used.

The images corresponding to the desired and initial camera positions are given in Figures 10(a) and 10(b) respectively. The obtained trajectories in the image for the three experiments are given in the Figures 11(a), 11(b) and 11(c) respectively.

As expected, the trajectory of each point in the image is a straight line when a correct calibration is used (see Figure 11(a)). But in presence of modeling errors, we note that the trajectories are very far away from the expected ones (see Figure 11(b)). The motion of the points in the image are thus unpredictable and a part of the image features may get out of the camera field of view. As can be seen in Figure 11(c), by using a variable reference, the expected trajectories are really obtained even if important modeling errors are introduced. The motion of each point in the image are thus perfectly predictable. This experiment confirms that a trajectory following in the image space gives better results than a point-to-point motion and improves significantly the robustness with respect to modeling errors.
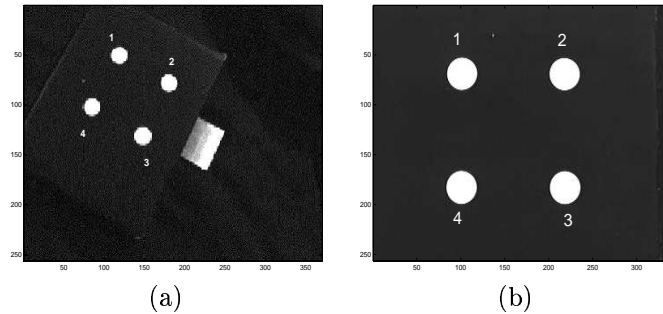
Figure 10: (a) Initial, (b) desired images of the target
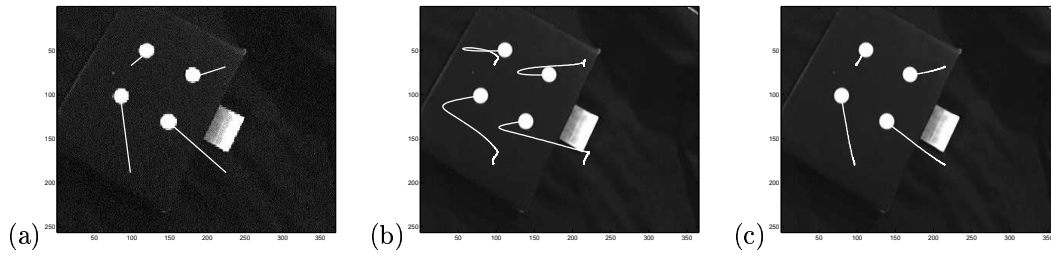
Figure 11: Trajectories in the image when: (a) a constant reference $\mathbf{s}^*$ and a perfect camera calibration are used; (b) a constant reference $\mathbf{s}^*$ is used and a 40% error on the intrinsic parameters is introduced; (c) a variable reference $\mathbf{s}^*(t)$ is used and a 40% error on the intrinsic parameters is introduced

7.2 Experimental results for a known planar object

We again consider a planar object with four white marks. The images corresponding to the desired and initial camera positions are given in Figures 12(a) and 12(b) respectively. The corresponding camera displacement between the desired and the initial camera frames is very important ($t_x = 300$mm, $t_y = 550$mm, $t_z = 120$mm ($\mathbf{u}\theta)_x = 28$dg, ($\mathbf{u}\theta)_y = 78$dg, ($\mathbf{u}\theta)_z = 147$dg) and, in this case, classical image-based and position-based visual servoing fail. In order to emphasize the importance of the introduced constraint in the trajectories, we perform the path planning of the target without repulsive potential (see Figure 12(c)). We observe that the visual features largely get out of the camera field of view.
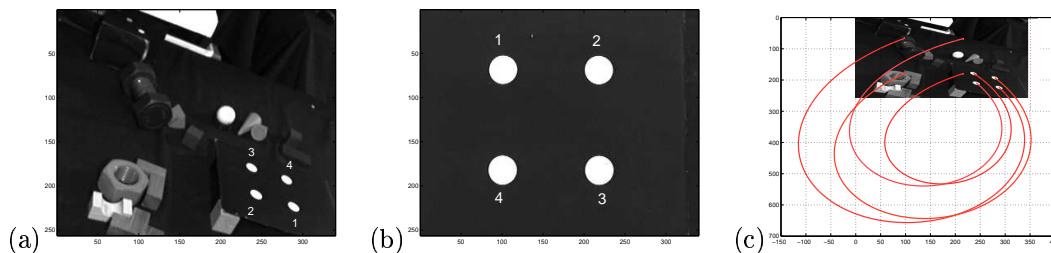
Figure 12: (a) Initial, (b) desired images of the target, (c) trajectories without repulsive potential

In the experiment whose results are reported in Figure 13, the intrinsic parameters given by the camera manufacturer are used. The 3-D parameters used as initialization of the path planning algorithm (that is the initial and desired camera poses) have been obtained by coupling the Dementhon algorithm [4] and the Lowe algorithm [11]. Planned and tracked trajectories are plotted in Figures 13(a) and 13(b) respectively. We can notice that the tracked trajectories and the planned trajectories are almost similar. This shows the efficiency

of our control scheme. The tracking error $(\mathbf{s}(t) - \mathbf{s}^*(t))$ is plotted in Figure 13(e), and it confirms the previous comment since the maximal error is always less than 5 pixels. The error on the coordinates of each target point between its current and its desired location in the image $(\mathbf{s}(t) - \mathbf{s}^*)$ is given in Figure 13(d). The convergence of the coordinates to their desired value demonstrates the correct realization of the task. The computed control law is given in Figure 13(f). We can note its satisfactory variations due to the regularity of the error function. The 3-D camera trajectory is plotted in Figure 13(c).
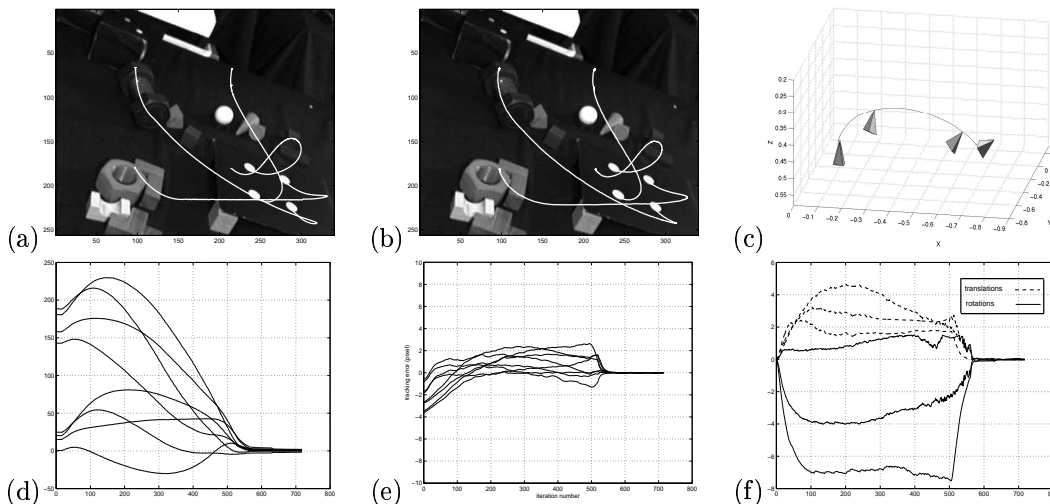
Figure 13: Experiment using the target model: (a) planned trajectories, (b) followed trajectories, (c) camera trajectory, (d) error in image points coordinates (pixels), (e) tracking error (pixels) and (f) velocities (cm/s and dg/s)

7.3 Experimental results for an unknown planar object

We now present the experimental results obtained without taking into account the knowledge of shape and dimension of the object. The initial and desired configurations are the same ones as those used in the previous experiment. The partial motion between the initial and desired camera positions, used to initialize the path planning algorithm is obtained from a projective reconstruction. As far as calibration is concerned, three different sets of parameters have been used:

1) *correct calibration:* the correct intrinsic parameters and value of d^* (that is 35 cm) have been used (see Figure 14);

2) *coarse calibration:* an error of 20% has been added on the intrinsic parameters, while d^* has been set to 20 cm (see Figure 15);

3) *bad calibration:* an error of 50% has been added on the intrinsic parameters, while d^* has been set to 70 cm (see Figure 16)

1) Correct calibration: First, we note that the trajectories obtained with or without using the object model are almost similar (refer to Figures 13 and 14). Once again, as can be seen in Figures 14(a) and 14(b) the planned and the tracked trajectories are also similar and the tracking error, given in Figure 14(e), remains small during the servoing (less than 5 pixels). Thus, the previous comments, in the case of a known model target, are also valid. The task is correctly realized. This is shown by the convergence of the image points coordinates to their desired value (see Figure 14(d)).

2) and 3) Coarse and Bad Calibrations: We now test the robustness of our approach with respect to calibration errors and errors on the parameter d^*. As can be seen in Figures 14(a), 14(b) and in Figures 15(a), 15(b), the planned and tracked trajectories in the cases of a correct and coarse calibration are similar. The trajectories obtained with bad calibration are close to those obtained in the other cases (see Figure 16). That confirms the robustness of the path planning and of the control scheme with respect to calibration errors and errors on d^*. The tracking error (Figure 15(c)) remains small in the coarse calibration case (less than 5 pixels). It remains satisfactory in the bad calibration case, since always less than 10 pixels (Figure 16(e)). In all the configurations, the tracking error remains sufficiently little to ensure a good behavior of the 2-D control scheme. We note the stability and the robustness of the control law (see Figures 14(f), 15(f) and 16(f)). Finally, we note that the task is correctly realized as well for the coarse calibration case as for the bad calibration case (refer to Figures 15(d) and 16(d)).
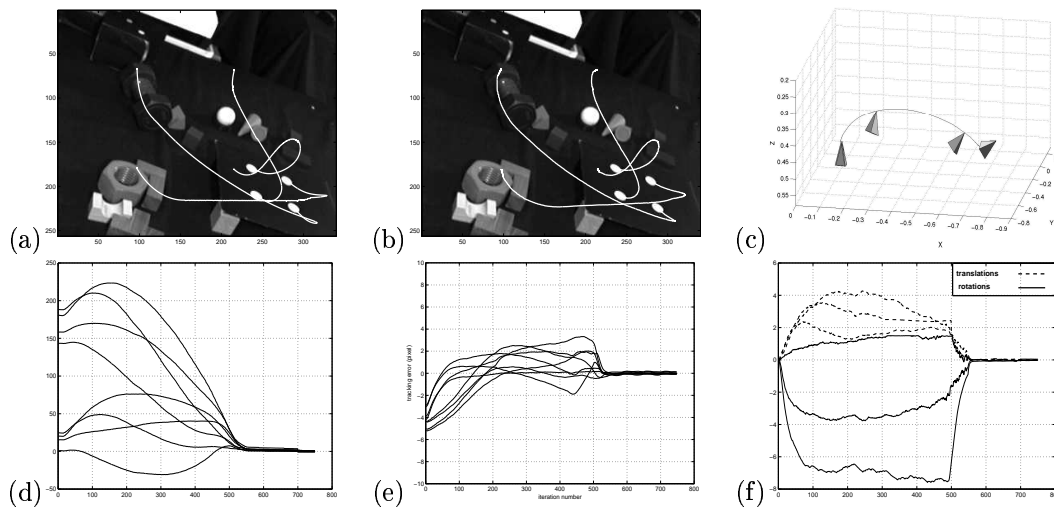

Figure 14: Same experiment without using the target model and using correct calibration: (a) planned trajectories, (b) followed trajectories, (c) camera trajectory, (d) error in image points coordinates (pixels), (e) tracking error (pixels) and (f) velocities (cm/s and dg/s)
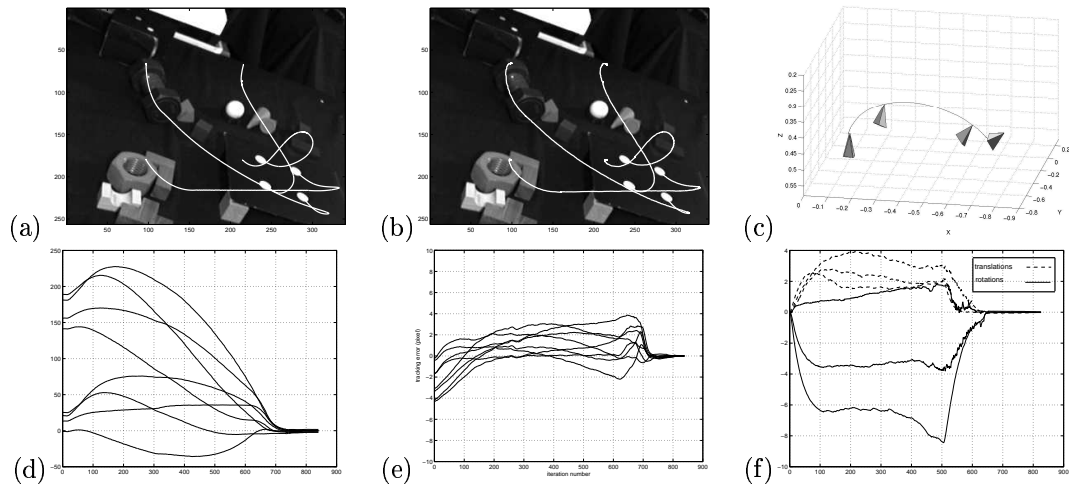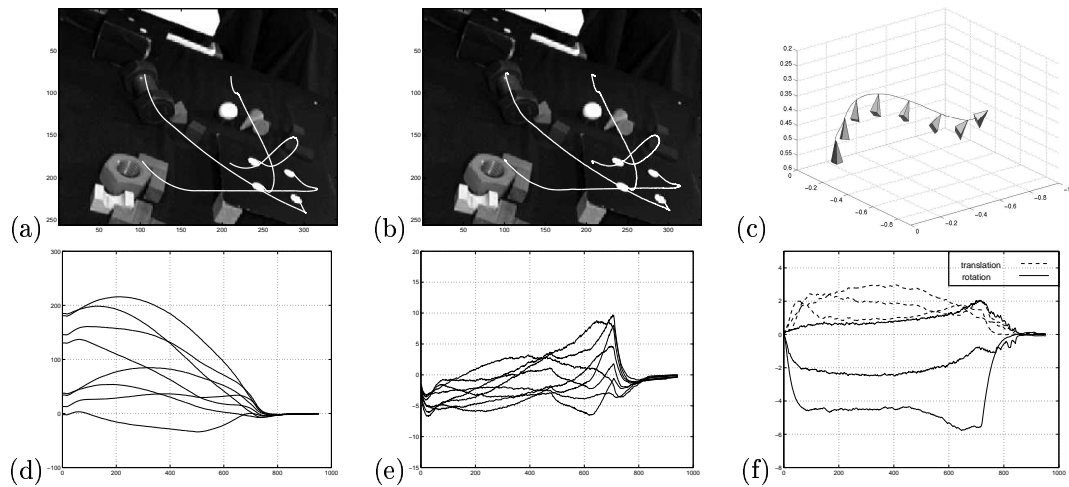
Figure 15: Same experiment using coarse calibration: (a) planned trajectories, (b) followed trajectories, (c) camera trajectory, (d)error in image points coordinates (pixels) (e) tracking error (pixels) and (f) velocities (cm/s and dg/s)
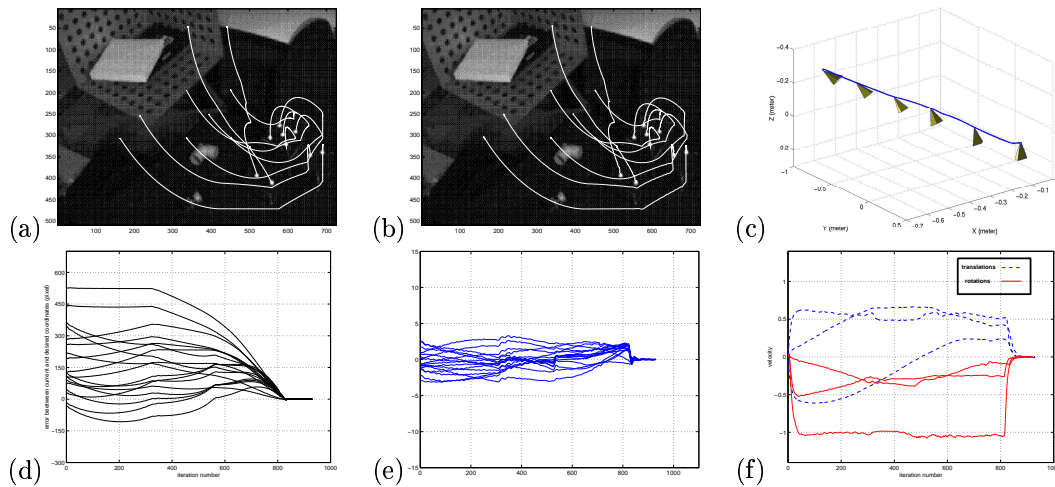

Figure 16: Same experiment using bad calibration: (a) planned trajectories, (b) followed trajectories, (c) camera trajectory, (d) error in image points coordinates (pixels), (e) tracking error (pixels) and (f) velocities (cm/s and dg/s)

7.4   Experimental results for an unknown non-planar object

The target is now composed of nine white marks lying on three different planes (see Figure 17). In this experiment, the camera displacement is very important ($t_x = -672mm$, $t_y = -1062mm$, $t_z = 468mm$, $(u\theta)_x = 30.6dg$, $(u\theta)_y = 56dg$, $(u\theta)_z = 137dg$). As previously, the path planning algorithm is initialized by using a projective reconstruction and a scaled Euclidean reconstruction. The same values of intrinsic parameters that in the case of a planar object have been used. The depth d^* has been set to 70cm, 50cm and 100cm in the cases of correct, coarse and bad calibration respectively. In this part, we only exhibit the results since the comments in the case of an unknown planar object are also valid here. However, we note, once again, that the results are satisfactory in the three cases.
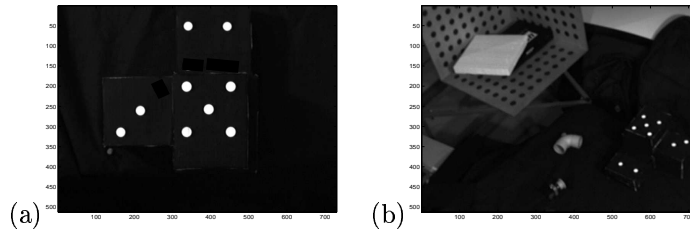
Figure 17: (a) Initial, (b) desired images of the target

Figure 18: Experiment with a non-planar object without using the target model and using correct calibration: (a) planned trajectories, (b) followed trajectories, (c) camera trajectory, (d) error in image points coordinates (pixels), (e) tracking error (pixels) and (f) velocities (cm/s and dg/s)
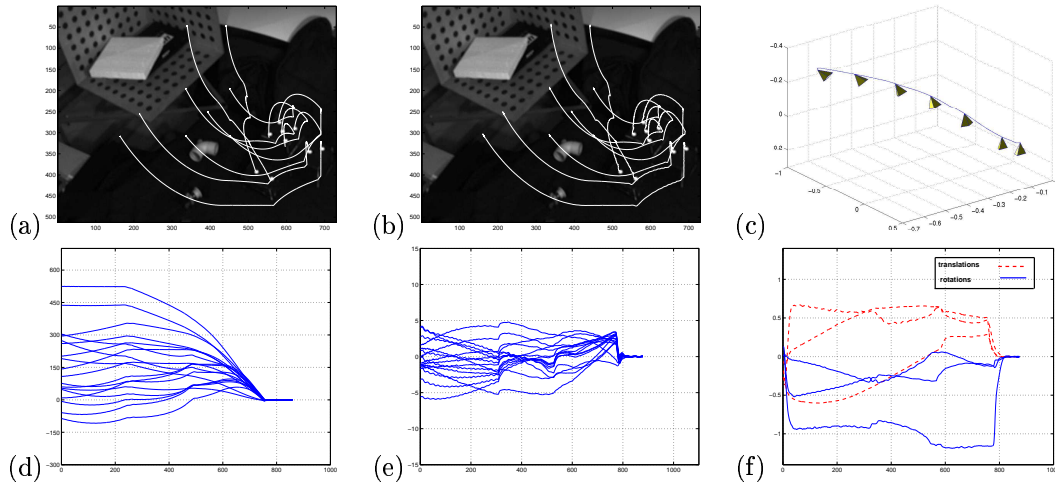
Figure 19: Same experiment using coarse calibration: (a) planned trajectories, (b) followed trajectories, (c) camera trajectory, (d) error in image points coordinates (pixels), (e) tracking error (pixels) and (f) velocities (cm/s and dg/s)
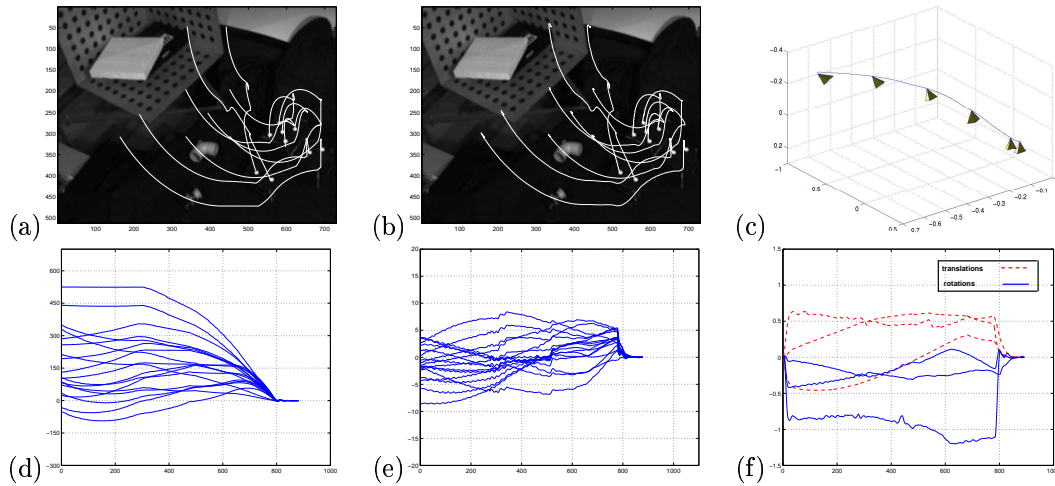

Figure 20: Same experiment using bad calibration: (a) planned trajectories, (b) followed trajectories, (c) camera trajectory, (d) error in image points coordinates (pixels), (e) tracking error (pixels) and (f) velocities (cm/s and dg/s)

7.5 Introducing joint limits avoidance

The images corresponding to the desired and initial camera positions are given in Figures 21(a) and 21(b) respectively. On all the following plots, joint positions are normalized between [-1;1], where -1 and 1 represent the joint limits.

We first perform the path planning without repulsive potential. The results are given in Figures 21(c) and 21(d). We can see that the visual features get out largely of the camera field of view and the axis q_5 attains its joint limit. Then, only the repulsive potential associated to the visibility constraint has been activated. In that case, even if the visibility constraint is ensured (Fig 21(e)) the servoing can not be realized because the axis q_5 reaches its joint limit (Fig 21(f)). In Figure 22, the two repulsive potentials are activated. The target remains in the camera field of view (see Figure 22(a) and 22(c)) and all axes avoid their joint limits (see Figure 22(b) and 22(d)). Once again, the positioning task is correctly realized.
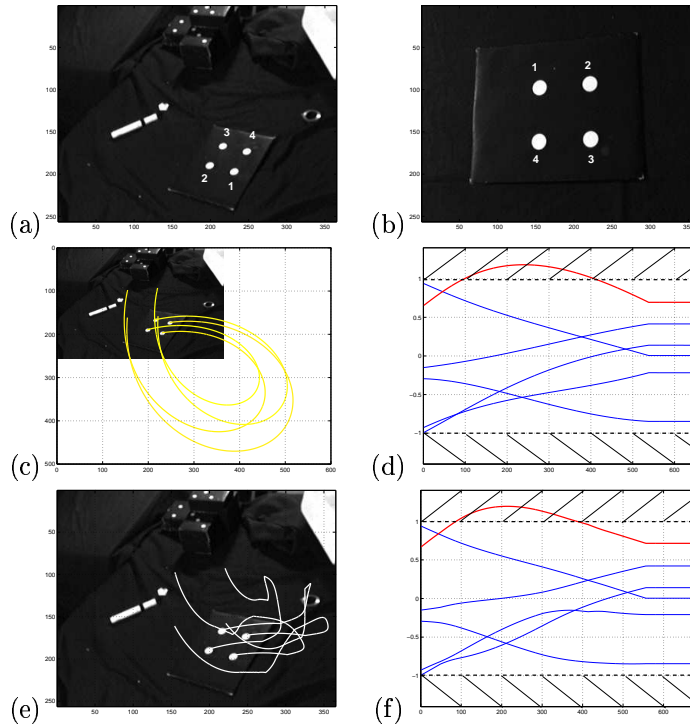

Figure 21: Initial (a) and desired (b) images; planned trajectories without repulsive potential: (a) in the image, (b) in the joint space; planned trajectories without repulsive potential associated to the joint limits avoidance: (c) in the image, (d) in the joint space
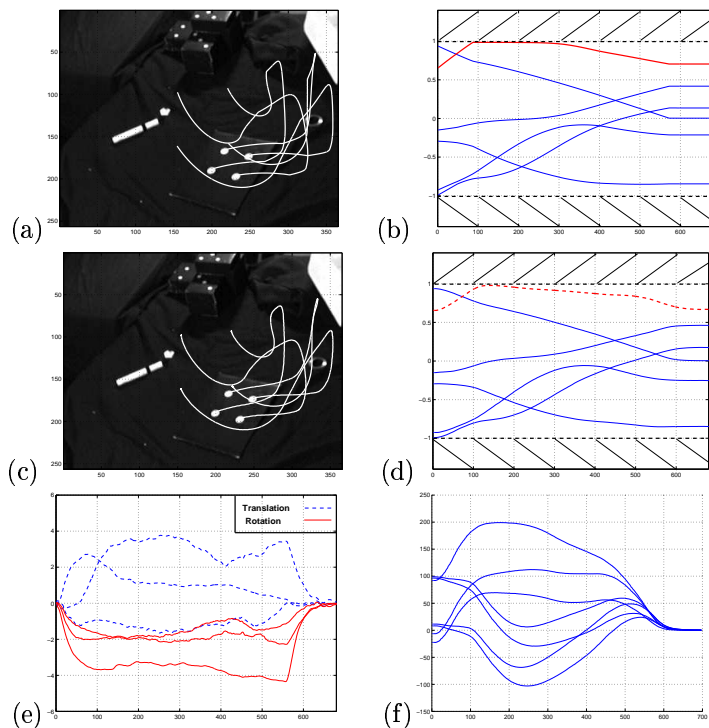
Figure 22: Planned trajectories with both repulsive potential: (a) in the image, (b) in the joint space; realized trajectories: (c) in the image, (d) in the joint space; (e) camera velocities (dg/s and cm/s) versus iteration number, (f) error in image point coordinates (pixels)

8   Conclusion

In this paper, we have presented a robust method ensuring the convergence for all initial camera positions. By coupling an image-based trajectory generator and an image-based servoing, the proposed method extends the well-known robustness and stability of image-based servoing when initial and desired camera location are close to the case where they are distant. The obtained trajectories provide some good expected properties: along these trajectories, the target remains in the camera field of view, the corresponding robot motion is physically realizable and the camera trajectory is a straight line outside the area where the repulsive forces are needed. Experimental results show the validity of our approach and its robustness with respect to modeling errors. Future work will be devoted to generate the trajectories in image space of more complex features than n points in order to apply our method to natural objects.

References

[1] F. Chaumette. Potential problems of stability and convergence in image-based and position-based visual servoing. *The Confluence of Vision and Control, D. Kriegman, G. Hager, A. Morse (eds), LNCIS Series, Springer Verlag*, 237:66–78, 1998.

[2] F. Chaumette and E. Marchand. A new redundancy-based iterative scheme for avoiding joint limits: Application to visual servoing. In *IEEE Int. Conf. on Robotics and Automation*, volume 2, pages 1720–1725, San Francisco, California, April 2000.

[3] N.J. Cowan and D.E. Koditschek. Planar image based visual servoing as a navigation problem. In *IEEE Int. Conf. on Robotics and Automation*, pages 611–617, Detroit, Michigan, May 1999.

[4] D. Dementhon and L.S. Davis. Model-based object pose in 25 lines of code. *Int. Journal of Computer Vision, 15(1/2): 123-141*, June 1995.

[5] O. Faugeras and F. Lustman. Motion and structure from motion in a piecewise planar environment. *Int. Journal of Pattern Recognition and Artificial Intelligence*, 2(3):485–508, 1988.

[6] K. Hashimoto. *Visual Servoing: Real Time Control of Robot Manipulators Based on Visual Sensory Feedback*. World Scientific Series in Robotics and Automated Systems, Vol 7,World Scientific Press, Singapor, 1993.

[7] K. Hosoda, K. Sakamoto, and M. Asada. Trajectory generation for obstacle avoidance of uncalibrated stereo visual servoing without 3d reconstruction. *IEEE/RSJ Int. Conf. on Intelligent Robots and Systems*, 1(3):29–34, August 1995.

[8] S. Hutchinson, G.D. Hager, and P.I. Corke. A tutorial on visual servo control. *IEEE Trans. on Robotics and Automation*, 12(5):651–670, October 1996.

[9] O. Khatib. Real time obstacle avoidance for manipulators and mobile robots. *Int. Journal of Robotics Research*, 5(1):90–98, 1986.

[10] J. C. Latombe. *Robot Motion Planning*. Kluwer Academic Publishers, 1991.

[11] D. G. Lowe. Fitting parameterized three-dimensional models to image. *IEEE Trans. on Pattern Analysis and Machine Intelligence*, 13(5):441–450, May 1991.

[12] E. Malis and F. Chaumette. 2 1/2 d visual servoing with respect to unknown objects through a new estimation scheme of camera displacement. *Int. Journal of Computer Vision*, 37(1):79–97, June 2000.

[13] E. Malis, F. Chaumette, and S. Boudet. 2 1/2 d visual servoing. *IEEE Trans. on Robotics and Automation*, 15(2):238–250, April 1999.

[14] P. Martinet, N. Daucher, J. Gallice, and M. Dhome. *Robot control using monocular pose estimation.* Worshop on New Trends in Image-based Robot Servoing, IROS'97, Grenoble, 1997.

[15] Y. Mezouar and F. Chaumette. Path planning in image space for robust visual servoing. *IEEE Int. Conf. on Robotics and Automation*, 3:2759–2764, April 2000.

[16] B.J. Nelson and P.K. Khosla. Strategies for increasing the tracking region of an eye-in-hand system by singularity and joint limits avoidance. *Int. Journal of Robotics Research, 14(3):255-269*, June 1995.

[17] A. Ruf and R. Horaud. Visual trajectories from uncalibrated stereo. *IEEE Int. Conf. on Intelligent Robots and Systems*, pages 83–91, 1997.

[18] R. Singh, R. M. Voyle, D. Littau, and N. P. Papanikolopoulos. Alignement of an eye-in-hand system to real objects using virtual images. *Workshop on Robust Vision for Vision-Based Control of Motion, IEEE Int. Conf. on Robotics and Automation*, May 1998.

[19] L.E Weiss, A.C Sanderson, and C.P Neuman. Dynamic sensor-based control of robot with visual feedback. *IEEE Journal of Robotics and Automation*, 3(5):404–417, October 1987.

[20] W.J Wilson, C.C Williams Hulls, and G.S Bell. Relative end-effector control using cartesian position-based visual servoing. *IEEE Trans. on Robotics and Automation*, 12(5):684–696, 1996.